NANO LETTERS

Monoclinic $LaSb_2$ Superconducting Thin Films

Adrian Llanos, Giovanna Campisi, Veronica Show, Jinwoong Kim, Reiley Dorrian, Salva Salmani-Rezaie, Nicholas Kioussis, and Joseph Falson*

Cite This: *Nano Lett.* 2024, 24, 8518−8524 **Read Online**

ACCESS | Metrics & More | Article Recommendations | Supporting Information

ABSTRACT: Rare-earth diantimondes exhibit coupling between structural and electronic orders, which are tunable under pressure and temperature. Here we present the discovery of a new polymorph of $LaSb_2$ stabilized in thin films synthesized using molecular beam epitaxy. Using diffraction, electron microscopy, and first-principles calculations we identify a $YbSb_2$-type monoclinic lattice as a yet-uncharacterized stacking configuration. The material hosts superconductivity with a T_c = 2 K, which is enhanced relative to the bulk ambient phase, and a long superconducting coherence length of 1730 Å. This result highlights the potential thin film growth has in stabilizing novel stacking configurations in quasi-two-dimensional compounds with competing layered structures.

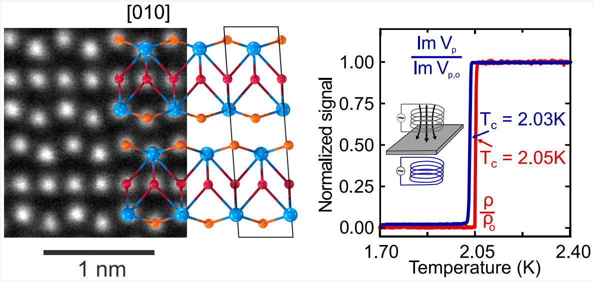

KEYWORDS: *thin-film growth, superconductivity, two-dimensional materials, rare-earth antimonide*

Layered intermetallics featuring the square-net structural motif form a versatile platform[1−4] for engineering electronic phases through chemical control over lattice symmetries[5−7] and stacking configurations.[8] Using common experimental tuning knobs such as chemical substitution, pressure (P) and temperature (T), it is known that structural configurations compete and can be modified with a subsequent influence on the flavor of the electronic ground state of the compound.[9−15] Antimony-based $LnSb_2$ (Ln = lanthanide element) materials form stoichiometric crystals, and refined structural analysis[16] describes the unit cell as being formed by two quintuple layer (QL) blocks, each consisting of two Ln-Sb corrugated layers sandwiching a two-dimensional Sb square net sheet. Variations in electron count on the square net Sb sites as determined by the rare-earth ionization state leads to a variety of bonding and stacking arrangements.[17] In the case of $EuSb_2$, the Eu^{2+} valence state causes a distortion of the Sb square net into zigzag chains and a monoclinic crystal structure,[18,19] while the orthorhombic structure of $YbSb_2$ is stabilized[20] by a small admixture of Yb^{3+} ions within a predominantly 2+ network.[21] Finally, in the case of (La, Ce, Nd, Sm)Sb_2 compounds, the 3+ valence again gives rise to an orthorhombic crystal in the so-called $SmSb_2$ structure type.[16,22] This latter structure differs from the $YbSb_2$ in the stacking arrangement of QL along the c-axis direction, which can be conceptualized by a displacement vector $\vec{d}$ within the $a-b$ plane, as illustrated in Figure 1a.

$LaSb_2$ stands out as a particularly sensitive structure that is susceptible to electronic and structural instabilities when tuning T and P. Bulk crystals grown with the self-flux method[23] form large, micaceous crystals with high residual resistivity ratios (RRR)[22,24] and nonsaturating positive magnetoresistance (MR).[22,25] Pronounced hysteretic electrical resistance when sweeping T is resolved under ambient P conditions.[15,26−28] Under application of moderate P, the hysteretic feature is suppressed to low T and is completely absent by $P \approx 12$ kbar. Accompanying this suppression is a sharpening of the superconducting (SC) transition under P and an increase in SC critical temperature (T_c) to a maximum of $T_c \approx 2$ K.[15,29,30] However, due to the micacity of crystals, reliable structural analysis at high P remains challenging and therefore complicates a full understanding of correlation between structural and electronic properties.

Molecular-beam epitaxy (MBE) as a synthesis technique has found much application in the engineering of low-temperature electronic ground states primarily through dimensional confinement[31−34] and epitaxial strain.[35−37] We use this technique to synthesize and study $LaSb_2$ thin films on MgO (001) (space group $Fm\bar{3}m$, a = 4.21 Å). Despite the lattice constants being relaxed in the (001)-oriented films, we discover a not previously observed crystal structure derived from the $YbSb_2$ structure type with an additional monoclinic shear. First-principles calculations suggest this layering arrangement as the lowest energy state, even compared to the observed $SmSb_2$ structure type of $LaSb_2$ single crystals

Received: March 1, 2024
Revised: June 25, 2024
Accepted: June 26, 2024
Published: July 1, 2024

https://doi.org/10.1021/acs.nanolett.4c01068

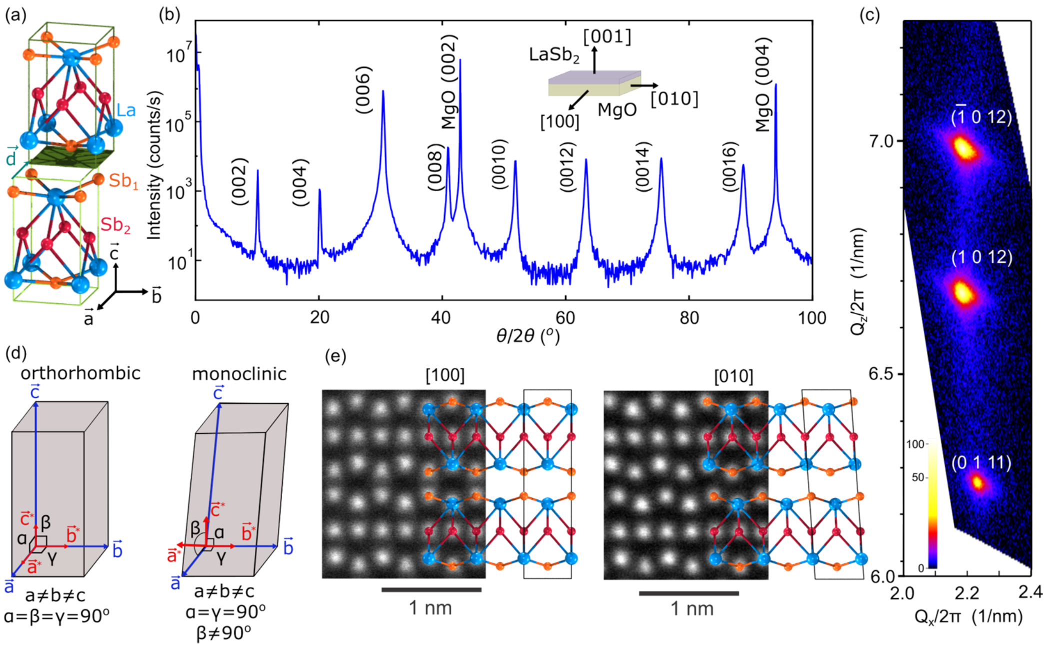

Figure 1. (a) Two QL building blocks of LaSb$_2$, where the upper QL block is shifted relative to the lower one by lateral displacement. (b) $\theta/2\theta$ diffraction pattern from LaSb$_2$. (c) Reciprocal space map taken along the h = 1 rod. Splitting at finite Q_x indicates a monoclinic tilt. (d) Schematic unit cells of the orthorhombic and monoclinic crystal systems. (e) Atomic arrangements obtained in transmission electron microscopy within domains with an overlay of the calculated unit cell modified with experimental lattice constant values.

commonly observed in bulk crystals. The electronic structure is characterized as a multiband system with one hole-like band derived from the La−Sb corrugated layer and multiple electron-like bands from the Sb sheet. The films display no resistance anomaly at high T indicative of a structural phase transition and are superconducting with a T_c = 2.03 K, which is enhanced relative to the bulk ambient where $T_c \approx 1$ K. The ability to stabilize stacking configurations of quasi-2D materials not observed in their bulk counterparts emphasizes the extra degrees of freedom available to thin film synthesis of this broad class of materials.

The structure of LnSb$_2$ materials is composed of QL blocks, which can form a variety of stacking configurations depending on their relative displacement.[16,20] This is depicted in Figure 1a with the vector $\vec{d}$, which represents the displacement in the a−b plane. Each QL contains one rare earth site, in this case La (blue), and two different Sb sites, noted as Sb$_1$ (orange) and Sb$_2$ (red) in Figure 1a. Out-of-plane X-ray diffraction of films presented in Figure 1b shows a single-phase, c-axis oriented film with a lattice parameter of c = 17.62 Å. This value is compressed relative to the value found in bulk LaSb$_2$ in the SmSb$_2$ structure where c = 18.56 Å.[16] A film of thickness t = 144 nm was used for determination of the lattice parameters. Rocking curve analysis reveals a full-width-half maximum of 0.03°, indicating low mosaicity, and a φ-scan using the (0 1 9) reflection reveals a $[100]_{LaSb_2} \parallel [100]_{MgO}$ epitaxial relationship with additional domains oriented $[100]_{LaSb_2} \parallel [110]_{MgO}$ (Figure S2).

Asymmetric reciprocal space mapping (RSM) (Figure 1c) along the h = 1 truncation rod was used to determine the in-plane lattice constants. The data reveal a twinned crystal structure with sets of spots corresponding to values from the two different crystal axes. For reflections corresponding to the a-axis, a pair of spots ((1 0 12) and ($\bar{1}$ 0 12)) are observed, whereas intensity at (0 1 11) is associated with diffraction from the b-axis. To simplify comparison with similar, bulk crystal polymorphs, we adopt a setting where the c-axis is taken to be the long axis. The corresponding a- and b-axis lattice constants were found to be a = 4.52 Å and b = 4.43 Å. The similarity of the lattice constant values for the grown film ($\frac{a-b}{a} \approx 2\%$) and their ≈6% mismatch with the cubic MgO substrate result in a relaxed film with twinned domains wherein both a- and b-axes predominantly align with the ⟨100⟩ directions of the substrate. For comparison, the bulk ambient phase adopts the SmSb$_2$ structure (space group No. 64 $Cmca$) with $a = b$ = 4.42 Å, γ = 91.27°.

The distribution of the (1 0 12) and ($\bar{1}$ 0 12) spots along $\vec{Q}_z$ reveals a monoclinic structure for the crystal, which can be understood by referring to Figure 1d. When a crystal distorts from orthorhombic to monoclinic, the $\vec{a^*}$ reciprocal lattice vector forms a finite angle with $\vec{a}$ so as to maintain orthogonality with $\vec{c}$. The reduced symmetry of the monoclinic structure relative to the MgO substrate leads to domains oriented 180° with respect to each other and the appearance of both ($h0l$) and ($-h0l$) reflections along the same direction. Thus, a single spot corresponding to ($h0l$) in the case of an orthorhombic crystal appears to "split" along $\vec{Q}_z$ into two spots corresponding to the two rotated domains. The angle between either of these spots and the horizontal can be used to determine the monoclinic tilt, which we find to be β = 85.95°.

Observed extinction conditions (Figure S3) imply an A-centered monoclinic cell and are consistent with three possible space groups (No. 12 $A2/m$, No. 5 $A2$, No 8 Am).[38] In Figure 1e we present a pair of scanning transmission electron microscopy (STEM) images labeled by the zone axis of the crystalline material. An extended set of micrographs is presented in the Supporting Information, showing that domains occur in varying proportions randomly in the sample, consistent with the X-ray data. Energy dispersive X-ray spectroscopy taken in the TEM (Figure S10) confirms the

1:2 La:Sb stoichiometry within an accepted tolerance of ≈10% for EDX in STEM.[39,40] Line cuts along Sb layers (Figure S11) reveal that Sb sheets form planar layers in contrast to the puckered layers found in the $YbSb_2$ structure.[20] Our proposed crystal structure was obtained from density functional theory calculations, to be discussed in the next section. In Figure 1e we overlay the calculated structure on the TEM images with lattice parameters taken from experiment, confirming the proposed atomic arrangements. The space group for the $LaSb_2$ films was determined to be No. 12 *A*2/*m*.

The stacking arrangements for these materials can be constructed from QL building blocks as shown in Figure 1a, where the upper block is shifted relative to the lower one by a displacement vector $\vec{d} = (d_x a_0,\ d_y b_0)$. This construction is possible because of the relatively weak bond between neighboring La−Sb layers, substantiated by the lower cleavage energy (Figure S4) and the longer interblock La−Sb bond length (>3.5 Å) compared to those of the intrablock bonds. The energy landscape of the two $LaSb_2$ building blocks on the two-dimensional $(d_x,\ d_y)$ displacement space is shown in Figure 2a. This is obtained using a relaxed unit block slab where $a_0 = b_0 = 4.50$ Å are the calculated equilibrium in-plane lattice constants, and shifting it relative to an adjacent slab, with subsequent relaxation of the atomic positions. The calculations reveal (i) four global energy minima, $Y^{\pm}$, and (ii) six saddle points, Y^0 and $S^{\pm}$. We note that the energy map preserves the C_4 rotational symmetry, inherited from the building block $(a_0 = b_0)$. It is evident that the vertical stacking $(d_x,\ d_y) = (0,\ 0)$ is not favored. The $S^{\pm}$ sites, $(d_x,\ d_y) = (\pm 0.25,\ \pm\ 0.25)$, correspond to the displacement of the Sm-type $LaSb_2$ structure (space group No. 64, *Cmca*) consisting of building blocks with a stacking sequence of $\cdots S^+S^-S^+S^-\cdots$ (see also Table 1). The Yb-type structure (space group No. 63, *Cmcm*) can also be explained with the stacking sequences of $\cdots Y^0Y^0Y^0Y^0\cdots$. The two displacements between three consecutive building blocks are illustrated in Figure 2b and c for the Sm- and Yb-type structures, where the successive lateral displacements are compensated and both Sm- and Yb-type structures preserve orthorhombicity. The tetragonal symmetry is broken in Sm- and Yb-type $LaSb_2$ due to the displacement of stacking sites that breaks the C_4 symmetry of the building block. Both phases, however, do not contain the lowest energy stacking arrangement $Y^{\pm}$ according to these calculations. Figure 2d shows one potential structure with repeating Y^+ stacking, $\cdots Y^+Y^+Y^+Y^+\cdots$, where the noncompensating displacement along the $\hat{x}$ direction leads to shear deformation of the out-of-plane lattice vector, rendering the system monoclinic. To further validate this method, we also have applied it to the $SmSb_2$ and $YbSb_2$ structures and have found the expected stacking arrangements are reproduced (Figure S5).

Table 1 lists the calculated relative total energies of the different stacking sequences, as well as experimentally obtained values for bulk crystals[16] and our thin films. The calculations point to the monoclinic structure (Yb-mono) as the ground state, with the previously synthesized Sm-type or proposed Yb-type phases exhibiting higher total energies. We note, however, that this is the energy at $T = 0$ and therefore is distinct from the free energy at elevated temperatures which contains phononic, magnetic, and electronic entropic contributions. The novel Yb-mono phase is consistent with the MBE-grown $LaSb_2$ structure where all the calculated lattice constants and monoclinic angle β agree well with the diffraction data within an error of 1%. Combining diffraction, calculation, and microscopy results, we unambiguously confirm the novel Yb-mono polymorph has been stabilized.

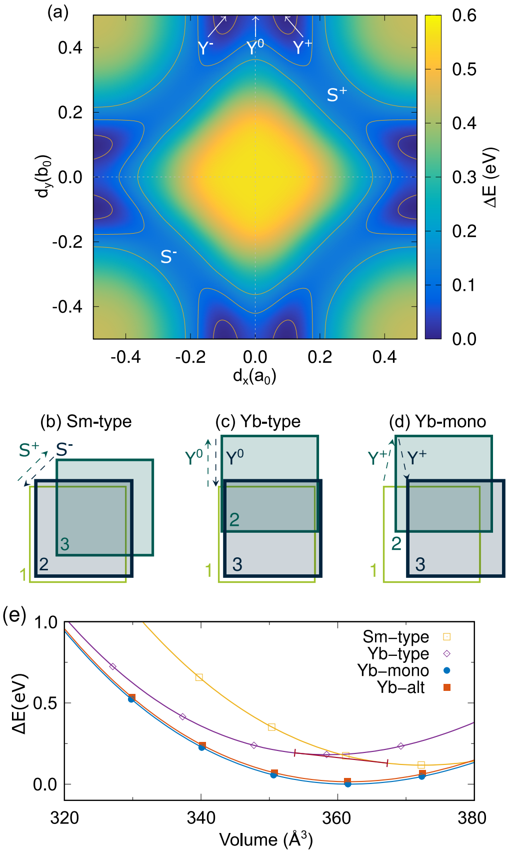

Figure 2. (a) Energy landscape of sliding two $LaSb_2$ QL building blocks in Figure 1a on the two-dimensional $(d_x,\ d_y)$ displacement space. The global energy minima are denoted by $Y^{\pm}$ and the saddle points by $S^{\pm}$ and Y^0. (b−d) Schematic top view of three $LaSb_2$ building blocks with different stacking sequences. The cell with label 1 denotes the bottom block. (b) Sm-type orthorhombic structure with alternating stacking sites of $[S^+S^-]$; (c) Yb-type orthorhombic structure with a sole stacking site of $[Y^0]$; and (d) Yb-like monoclinic structure with a sole stacking site of $[Y^+]$ resulting in a tilted out-of-plane lattice vector. (e) Total energies versus volume for the four crystal structures, where the solid curves are fits to the Birch−Murnaghan equation of state.

The calculations also reveal a new orthorhombic phase (Yb-alt in Table 1, space group No. 58, *Pnnm*) with alternating stacking sequences of $\cdots Y^+Y^-Y^+Y^-\cdots$, which is close in energy to the ground state Yb-mono structure. In order to study the relative stability of the four crystal structures under hydrostatic pressure, we show in Figure 2e the calculated total energies as a function of volume. We find that the Yb-mono structure remains the ground state under hydrostatic pressure, which on the other hand induces a structural phase transition from the Sm-type to the Yb-type structures at 0.749 GPa, close to the calculated value in ref 15 of ≃0.5 GPa.

In Figure 3a we present temperature dependence of resistivity for a film of thickness $t = 144$ nm. The films show metallic $\rho(T)$ with an RRR $(R_{300\text{ K}}/R_{2.5\text{K}})$ of 26. No features with sharp changes in $d\rho/dT$ are observed up to $T = 400$ K, which would indicate the presence of a CDW transition or first-order structural transition. In Figure 3b and 3d, the symmetrized magnetoresistance (MR) and antisymmeterized Hall resistivity up to fields of $B = 9$ T for several temperatures

Table 1. Calculated Relative Total Energies, Lattice Constants, and Angles of Several $LaSb_2$ Bulk Phases Corresponding to Different Stacking Sequences[a]

system	stacking sequence	SG	ΔE (meV/La)	a (Å)	b (Å)	c (Å)	α (deg)	β (deg)	γ (deg)
Sm-type	$\cdots S^+S^-S^+S^-[S^+S^-]\cdots$	64	29	4.470	4.470	18.628	90.0	90.0	91.1
Yb-type	$\cdots Y^0Y^0Y^0Y^0Y^0[Y^0]\cdots$	63	45	4.477	4.546	17.607	90.0	90.0	90.0
Yb-alt	$\cdots Y^+Y^-Y^+Y^-[Y^+Y^-]\cdots$	58	4	4.555	4.480	17.717	90.0	90.0	90.0
Yb-mono	$\cdots Y^+Y^+Y^+Y^+Y^+[Y^+]\cdots$	12	0	4.562	4.483	17.711	90.0	86.3	90.0
bulk exp.		64		4.42	4.42	18.56	90.0	90.0	91.2
this work		12		4.52	4.43	17.62	90.0	85.96	90.0

[a] SG indicates the space group. The Sm-type structure is a base-centered orthorhombic cell, and the lattice constants, a and b, are equivalent to the distance from the corner to the center of the conventional cell base.

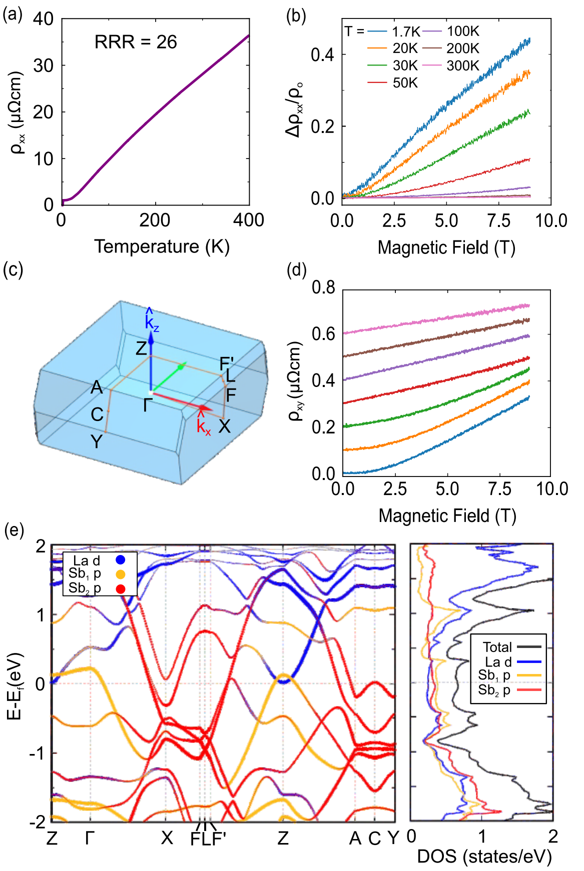

Figure 3. (a) Temperature-dependent longitudinal resistance. (b) Longitudinal magnetoresistance at different temperatures. (c) Brillouin zone and relevant high-symmetry points of the monoclinic structure. (d) Hall resistance curves at different temperatures, offset for clarity. (e) Calculated band structure with color-coded dispersion features associated with projections on various atomic sites, along with the corresponding DOS (total DOS scaled by $\frac{1}{4}$).

are given. The curvature of the Hall resistance indicates multiple carrier types while the MR displays linear behavior at high fields at low temperature, similar to bulk crystal data both in ambient conditions and under applied pressure, albeit with a reduced magnitude compared to bulk crystals.[22,25] Two carrier Drude fits[41] were applied to the MR data but were not found to capture the behavior at low temperature (Figure S7).

In Figure 3c we plot the Brillouin zone of the monoclinic crystal structure with the relevant high-symmetry points. The band structure along the high-symmetry directions (orange path in (c)) and the corresponding orbital-projected density of states (DOS) are displayed in Figure 3e, where the blue, orange, and red colors denote projections on the La-5d, Sb_1/5p, and Sb_2/5p orbitals (Sb_1 are on the La/Sb corrugated layer and Sb_2 are on the 2D Sb sheets in Figure 1a). The highly dispersing Sb_1/5p and Sb_2/5p bands crossing the Fermi level along the Γ−X and F′−Z directions indicate high carrier mobility along the in-plane directions similar to those in the bulk orthorhombic $LaSb_2$ structure[28,42,43] and in other topological square-net materials.[3] The presence of both hole-like and electron-like pockets at the Fermi level is in agreement with the observation of multiple carrier types from the Hall measurements.

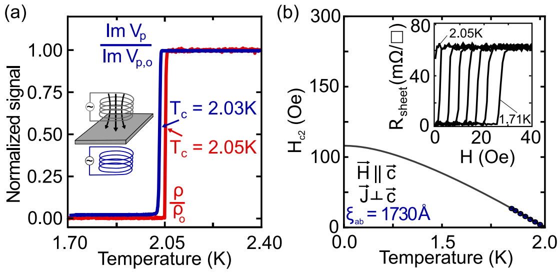

Figure 4. (a) Superconductivity measured in a 144 nm film via resistance (red) and mutual inductance (blue) methods. (b) Critical field as a function of temperature with WHH fit to extrapolate to zero temperature. Inset: a subset of critical field isotherms, taken approximately every 50 mK, between 2.05 K and 1.71 K.

In Figure 4a we present data showing the presence of a sharp superconducting transition with resistive $T_c \approx 2.05$ K. The films display zero resistance and flux expulsion, as evidenced by a drop in voltage on the secondary coil in a mutual inductance experimental geometry (inset of 4a). The measured T_c in the two experiments agree within 1%. In 4b, we plot the perpendicular critical field as a function of temperature. Determination of H_{c2} was performed by fitting the resistive transition isotherms to a sigmoid function $\rho = \frac{\rho_o}{1+\exp(-k(H-H_{c2}))}$ (see Methods). Data were taken every 25 mK between 2.05 and 1.71 K. The full set of critical field isotherms and fits is given in Figure S12. We extrapolate to zero temperature by fitting the data using the single-band, Werthamer, Helfand, and Hohenberg (WHH) formula[44] in the limit where orbital pair-breaking effects dominate spin paramagnetic and spin−orbit effects. We use the extrapolated value for $H_{c2\perp}(0) \approx 110$ Oe to estimate the coherence length, which gives $\xi_{ab} = \sqrt{\frac{\Phi_o}{2\pi H_{c2\perp}(0)}} = 1730$ Å. For comparison, a single-band Ginzburg−Landau model[45] gives $\xi_{ab} = 1400$ Å. These values are in agreement with the findings in bulk crystals under pressure.[30] The inset of 4b displays a subset of the isotherms used in the fitting and further demonstrates the sharpness of the transition.

One possibility for the stabilization of the monoclinic $LaSb_2$ is related to epitaxial strain or other perturbations induced by the substrate. The square symmetry of the MgO substrate would tend to favor layers with reduced orthorhombicity and lattice mismatch with the substrate. In the monoclinic phase, the *a*- and *b*-axes differ by ≈2% compared to approximately ≈2.5% for the ambient phase structure. However, the large lattice mismatch of ≈6% for the monoclinic structure makes it unlikely that coherent strain persists in the epilayer beyond the first 1−2 QL and therefore unlikely that the monoclinic structure is stabilized by epitaxial strain. Another possibility for the observation of the monoclinic phase in thin films, yet not in the bulk crystals, is the lower growth temperature used in the MBE growth processes ($\approx 500\ ^\circ C < T_{melt} = 630\ ^\circ C$).[46] During flux growth, crystals are obtained by slowly cooling the melt from the liquidus temperature (≈1000 °C), over a period of tens of hours and decanting the liquid flux slightly above the solidification temperature of the desired phase.[23] Given the results of the 0 K DFT simulations, monoclinic $LaSb_2$ may therefore be a low-temperature crystalline phase that would be preferentially stabilized by the vapor−solid reaction of MBE.

As of the time of writing, no single-crystal diffraction data have been reported for bulk-$LaSb_2$ at high *P*. The micacity of crystals makes such experiments challenging. Previous studies[15] have proposed $YbSb_2$ as a candidate structure for the high-*P* phase on the basis of DFT calculations. Our calculations agree that while the $YbSb_2$ structure is more stable compared to the $SmSb_2$ structure under pressure, the monoclinic Y^+ structure is the ground state. We propose that the application of pressure results in a structural transition to either the Y^+ polymorph or similar orthorhombic structure labeled $[Y^+Y^-]$, which is nearly degenerate. The association of the Y^+ phase with the high-pressure phase of the bulk crystal is further bolstered by the absence of resistance anomalies at high temperature and a sharp superconducting transition at 2 K. In bulk $LaSb_2$, the superconducting transition is broad, with onset temperatures of about $T = 2$ K, yet only reaching a fully superconducting state at $T = 0.4{-}0.5$ K.[30] Scanning tunneling microscopy experiments have suggested that the superconductivity is more robust at the surface with a measured T_c of 1.2 K.[47] The transition sharpens with *P* with concomitant suppression of the high-temperature resistance anomaly.[15,29] A maximum $T_c \approx 2$ K was observed under applied pressure of 4.5 kbar, at which point the anomaly is completely absent.[15,30] While the presence of a CDW transition in bulk $LaSb_2$ remains an open question[48] with recent studies[49] having found no evidence of a CDW gap opening, the strongly 2D-like Fermi surface in the other square-net systems such as $SmSb_2$-type $LaSb_2$ is not present in our structure (Figure S8 for discussion), which may play a role in the suppression of the resistance anomaly associated with a structural transition that competes with superconductivity. Further investigations into the superconducting phase will form the basis of future studies.

In summary, we have experimentally and theoretically presented a newly stable polymorph in the family of rare-earth diantimonides in thin films of $LaSb_2$ deposited on MgO (001). The films are superconducting with a critical temperature enhanced relative to reports on bulk crystals under ambient conditions. This study points toward this family of materials as a promising platform to study superconductivity with varying lattice motifs and layering orders that may be inaccessible or difficult to characterize in bulk samples.

ASSOCIATED CONTENT

Data Availability Statement

The data that support the findings of this study are available from the corresponding author upon reasonable request.

Supporting Information

The Supporting Information is available free of charge at https://pubs.acs.org/doi/10.1021/acs.nanolett.4c01068.

> Additional text including experimental sections on molecular beam epitaxy, X-ray diffraction, transmission electron microscopy, first-principles calculations, transport measurements, and mutual inductance measurements; additional figures of RHEED data for growth, rocking curve and ϕ-scan of films, additional reciprocal space maps of films, calculated cleavage energy of films, comparison of stacking for $SmSb_2$ and $YbSb_2$, wide range resistance scans of films, temperature-dependent magnetotransport, calculated Fermi surfaces, wide -area TEM image, elemental mapping of films, line profiles of TEM data, temperature dependence of the superconducting transition (PDF)

AUTHOR INFORMATION

Corresponding Author

Joseph Falson − *Department of Applied Physics and Materials Science, California Institute of Technology, Pasadena, California 91125, United States; Institute for Quantum Information and Matter, California Institute of Technology, Pasadena, California 91125, United States;* orcid.org/0000-0003-3183-9864; Email: falson@caltech.edu

Authors

Adrian Llanos − *Department of Applied Physics and Materials Science, California Institute of Technology, Pasadena, California 91125, United States; Institute for Quantum Information and Matter, California Institute of Technology, Pasadena, California 91125, United States;* orcid.org/0000-0002-5723-8007

Giovanna Campisi − *Department of Physics and W. M. Keck Computational Materials Theory Center, California State University, Northridge, Northridge, California 91330, United States*

Veronica Show − *Department of Applied Physics and Materials Science, California Institute of Technology, Pasadena, California 91125, United States; Institute for Quantum Information and Matter, California Institute of Technology, Pasadena, California 91125, United States*

Jinwoong Kim − *Department of Physics and W. M. Keck Computational Materials Theory Center, California State University, Northridge, Northridge, California 91330, United States;* orcid.org/0000-0003-3616-865X

Reiley Dorrian − *Department of Applied Physics and Materials Science, California Institute of Technology, Pasadena, California 91125, United States; Institute for Quantum Information and Matter, California Institute of Technology, Pasadena, California 91125, United States*

Salva Salmani-Rezaie − *Department of Materials Science and Engineering, The Ohio State University, Columbus, Ohio 43210, United States*

Nicholas Kioussis − *Department of Physics and W. M. Keck Computational Materials Theory Center, California State University, Northridge, Northridge, California 91330, United States*

Complete contact information is available at:
https://pubs.acs.org/10.1021/acs.nanolett.4c01068

Notes

The authors declare no competing financial interest.

■ ACKNOWLEDGMENTS

We thank Paul Canfield and Sergey Budko for helpful conversations and critical reading of the manuscript. J.F. acknowledges funding provided by the Air Force Office of Scientific Research (Grant number FA9550-22-1-0463), the Gordon and Betty Moore Foundation's EPiQS Initiative (Grant number GBMF10638), and the Institute for Quantum Information and Matter, an NSF Physics Frontiers Center (NSF Grant PHY-1733907). The work at CSUN acknowledges support from the NSF-PREP CSUN/Caltech-IQIM Partnership (Grant number 2216774) and NSF-PREM (Grant number DMR-1828019). We acknowledge the Beckman Institute for their support of the X-ray Crystallography Facility at Caltech. Electron microscopy was performed at the Center for Electron Microscopy and Analysis (CEMAS) at The Ohio State University.

■ REFERENCES

(1) Hoffmann, R.; Zheng, C. Making and breaking bonds in the solid state: The $ThCr_2Si_2$ structure. *J. Phys. Chem.* **1985**, *89*, 4175−4181.

(2) Kordyuk, A. A. Iron-based superconductors: Magnetism, superconductivity, and electronic structure (Review Article). *Low Temperature Physics* **2012**, *38*, 888−899.

(3) Klemenz, S.; Lei, S.; Schoop, L. M. Topological semimetals in square-net materials. *Annu. Rev. Mater. Res.* **2019**, *49*, 185−206.

(4) Yumigeta, K.; Qin, Y.; Li, H.; Blei, M.; Attarde, Y.; Kopas, C.; Tongay, S. Advances in rare-earth tritelluride quantum materials: Structure, properties, and synthesis. *Advanced Science* **2021**, *8*, 2004762.

(5) Ru, N.; Condron, C. L.; Margulis, G. Y.; Shin, K. Y.; Laverock, J.; Dugdale, S. B.; Toney, M. F.; Fisher, I. R. Effect of chemical pressure on the charge density wave transition in rare-earth tritellurides RTe_3. *Phys. Rev. B* **2008**, *77*, 035114.

(6) Ni, N.; Tillman, M. E.; Yan, J.-Q.; Kracher, A.; Hannahs, S. T.; Bud'ko, S. L.; Canfield, P. C. Effects of co substitution on thermodynamic and transport properties and anisotropic H_{c2} in $Ba(Fe_{1-x}Co_x)_2As_2$ single crystals. *Phys. Rev. B* **2008**, *78*, 214515.

(7) Lei, S.; Duppel, V.; Lippmann, J. M.; Nuss, J.; Lotsch, B. V.; Schoop, L. M. Charge Density Waves and Magnetism in Topological Semimetal Candidates $GdSb_xTe_{2-x-\delta}$. *Advanced Quantum Technologies* **2019**, *2*, 1900045.

(8) Straquadine, J. A. W.; Weber, F.; Rosenkranz, S.; Said, A. H.; Fisher, I. R. Suppression of charge density wave order by disorder in pd-intercalated $ErTe_3$. *Phys. Rev. B* **2019**, *99*, 235138.

(9) DiMasi, E.; Foran, B.; Aronson, M. C.; Lee, S. Stability of charge-density waves under continuous variation of band filling in $LaTe_{2-x}Sb_x$ ($0\leqslant x\leqslant 1$). *Phys. Rev. B* **1996**, *54*, 13587−13596.

(10) Shin, K. Y.; Brouet, V.; Ru, N.; Shen, Z. X.; Fisher, I. R. Electronic structure and charge-density wave formation in $LaTe_{1.95}$ and $CeTe_{2.00}$. *Phys. Rev. B* **2005**, *72*, 085132.

(11) Llanos, A.; Salmani-Rezaie, S.; Kim, J.; Kioussis, N.; Muller, D. A.; Falson, J. Supercell formation in epitaxial rare-earth ditelluride thin films. *Cryst. Growth Des.* **2024**, *24*, 115−121.

(12) Huang, Q.; Qiu, Y.; Bao, W.; Green, M. A.; Lynn, J. W.; Gasparovic, Y. C.; Wu, T.; Wu, G.; Chen, X. H. Neutron-diffraction measurements of magnetic order and a structural transition in the parent $BaFe_2As_2$ compound of feas-based high-temperature superconductors. *Phys. Rev. Lett.* **2008**, *101*, 257003.

(13) Xiang, L.; Ryan, D. H.; Straszheim, W. E.; Canfield, P. C.; Bud'ko, S. L. Tuning of charge density wave transitions in $LaAu_xSb_2$ by pressure and au stoichiometry. *Phys. Rev. B* **2020**, *102*, 125110.

(14) Singha, R.; Salters, T. H.; Teicher, S. M. L.; Lei, S.; Khoury, J. F.; Ong, N. P.; Schoop, L. M. Evolving devil's staircase magnetization from tunable charge density waves in nonsymmorphic dirac semimetals. *Adv. Mater.* **2021**, *33*, 2103476.

(15) Weinberger, T. I.; de Podesta, C. K.; Chen, J.; Hodgson, S. A.; Grosche, F. M. Pressure-dependent structural and electronic instabilities in $LaSb_2$. *SciPost Phys. Proc.* **2023**, 018.

(16) Wang, R.; Steinfink, H. The crystal chemistry of selected AB2 rare earth compounds with selenium, tellurium, and antimony. *Inorg. Chem.* **1967**, *6*, 1685−1692.

(17) Papoian, G. A.; Hoffmann, R. Hypervalent Bonding in One, Two, and Three Dimensions: Extending the Zintl−Klemm Concept to Nonclassical Electron-Rich Networks. *Angew. Chem., Int. Ed.* **2000**, *39*, 2408−2448.

(18) Hulliger, F.; Schmelczer, R. Crystal structure and antiferromagnetism of $EuSb_2$. *J. Solid State Chem.* **1978**, *26*, 389−396.

(19) Ohno, M.; Uchida, M.; Kurihara, R.; Minami, S.; Nakazawa, Y.; Sato, S.; Kriener, M.; Hirayama, M.; Miyake, A.; Taguchi, Y.; Arita, R.; Tokunaga, M.; Kawasaki, M. Quantum transport observed in films of the magnetic topological semimetal $EuSb_2$. *Phys. Rev. B* **2021**, *103*, 165144.

(20) Wang, R.; Bodnar, R.; Steinfink, H. The structure of $YbSb_2$, a zrsi2 isotype. *Inorg. Chem.* **1966**, *5*, 1468−1470.

(21) Tremel, W.; Hoffmann, R. Square nets of main-group elements in solid-state materials. *J. Am. Chem. Soc.* **1987**, *109*, 124−140.

(22) Bud'ko, S. L.; Canfield, P. C.; Mielke, C. H.; Lacerda, A. H. Anisotropic magnetic properties of light rare-earth diantimonides. *Phys. Rev. B* **1998**, *57*, 13624−13638.

(23) Canfield, P. C.; Fisk, Z. Growth of single crystals from metallic fluxes. *Philosophical Magazine B* **1992**, *65*, 1117−1123.

(24) Fischer, K. F. F.; Roth, N.; Iversen, B. B. Transport properties and crystal structure of layered $LaSb_2$. *J. Appl. Phys.* **2019**, *125*, 045110.

(25) Young, D. P.; Goodrich, R. G.; DiTusa, J. F.; Guo, S.; Adams, P. W.; Chan, J. Y.; Hall, D. High magnetic field sensor using $LaSb_2$. *Appl. Phys. Lett.* **2003**, *82*, 3713−3715.

(26) DiTusa, J. F.; Guritanu, V.; Guo, S.; Young, D. P.; Adams, P. W.; Goodrich, R. G.; Chan, J. Y.; van der Marel, D. Optical conductivity and superconductivity in $LaSb_2$. *Journal of Physics* **2011**, *273*, 012151.

(27) Luccas, R. F.; Fente, A.; Hanko, J.; Correa-Orellana, A.; Herrera, E.; Climent-Pascual, E.; Azpeitia, J.; Pérez-Castañeda, T.; Osorio, M. R.; Salas-Colera, E.; Nemes, N. M.; Mompean, F. J.; García-Heranández, M.; Rodrigo, J. G.; Ramos, M. A.; Guillamón, I.; Vieira, S.; Suderow, H. Charge density wave in layered $La_{1-x}Ce_xSb_2$. *Phys. Rev. B* **2015**, *92*, 235153.

(28) Palacio, I.; Obando-Guevara, J.; Chen, L.; Nair, M.; Barrio, M. G.; Papalazarou, E.; Le Fèvre, P.; Taleb-Ibrahimi, A.; Michel, E.; Mascaraque, A.; Tejeda, A. Fermi surface of $LaSb_2$ and direct observation of a cdw transition. *Appl. Surf. Sci.* **2023**, *610*, 155477.

(29) Bud'ko, S. L.; Huyan, S.; Herrera-Siklody, P.; Canfield, P. C. Rapid suppression of charge density wave transition in $LaSb_2$ under pressure. *Philos. Mag.* **2023**, *103*, 561−573.

(30) Guo, S.; Young, D. P.; Adams, P. W.; Wu, X. S.; Chan, J. Y.; McCandless, G. T.; DiTusa, J. F. Dimensional crossover in the electrical and magnetic properties of the layered $LaSb_2$ superconductor under pressure: The role of phase fluctuations. *Phys. Rev. B* **2011**, *83*, 174520.

(31) Zhang, W.-H.; Sun, Y.; Zhang, J.-S.; Li, F.-S.; Guo, M.-H.; Zhao, Y.-F.; Zhang, H.-M.; Peng, J.-P.; Xing, Y.; Wang, H.-C.; Fujita, T.; Hirata, A.; Li, Z.; Ding, H.; Tang, C.-J.; Wang, M.; Wang, Q.-Y.; He, K.; Ji, S.-H.; Chen, X.; Wang, J.-F.; Xia, Z.-C.; Li, L.; Wang, Y.-Y.; Wang, J.; Wang, L.-L.; Chen, M.-W.; Xue, Q.-K.; Ma, X.-C. Direct

Observation of High-Temperature Superconductivity in One-Unit-Cell FeSe Films. *Chin. Phys. Lett.* **2014**, *31*, 017401.

(32) Shiogai, J.; Ito, Y.; Mitsuhashi, T.; Nojima, T.; Tsukazaki, A. Electric-field-induced superconductivity in electrochemically etched ultrathin FeSe films on $SrTiO_3$ and MgO. *Nat. Phys.* **2016**, *12*, 42−46.

(33) Jeffrey Gardner, H.; Kumar, A.; Yu, L.; Xiong, P.; Warusawithana, M. P.; Wang, L.; Vafek, O.; Schlom, D. G. Enhancement of superconductivity by a parallel magnetic field in two-dimensional superconductors. *Nat. Phys.* **2011**, *7*, 895−900.

(34) Falson, J.; Xu, Y.; Liao, M.; Zang, Y.; Zhu, K.; Wang, C.; Zhang, Z.; Liu, H.; Duan, W.; He, K.; et al. Type-ii ising pairing in few-layer stanene. *Science* **2020**, *367*, 1454−1457.

(35) Bozovic, I.; Logvenov, G.; Belca, I.; Narimbetov, B.; Sveklo, I. Epitaxial strain and superconductivity in $La_{2-x}Sr_xCuO_4$ thin films. *Phys. Rev. Lett.* **2002**, *89*, 107001.

(36) Ruf, J. P.; Paik, H.; Schreiber, N. J.; Nair, H. P.; Miao, L.; Kawasaki, J. K.; Nelson, J. N.; Faeth, B. D.; Lee, Y.; Goodge, B. H.; et al. Strain-stabilized superconductivity. *Nat. Commun.* **2021**, *12*, 59.

(37) Engelmann, J.; Grinenko, V.; Chekhonin, P.; Skrotzki, W.; Efremov, D.; Oswald, S.; Iida, K.; Hühne, R.; Hänisch, J.; Hoffmann, M.; et al. Strain induced superconductivity in the parent compound $BaFe_2As_2$. *Nat. Commun.* **2013**, *4*, 2877.

(38) Flack, D. H. *International Tables For Crystallography*; International Union for Crystallography, 2016; Chapter 1.6, pp 114−128.

(39) Lugg, N.; Kothleitner, G.; Shibata, N.; Ikuhara, Y. *On the quantitativeness of eds stem, Ultramicroscopy* **2015**, *151*, 150. Special Issue: 80th Birthday of Harald Rose; PICO 2015 - Third Conference on Frontiers of Aberration Corrected Electron Microscopy.

(40) MacArthur, K. E.; Brown, H. G.; Findlay, S. D.; Allen, L. J. Probing the effect of electron channelling on atomic resolution energy dispersive x-ray quantification. *Ultramicroscopy* **2017**, *182*, 264−275.

(41) Luo, Y.; Li, H.; Dai, Y. M.; Miao, H.; Shi, Y. G.; Ding, H.; Taylor, A. J.; Yarotski, D. A.; Prasankumar, R. P.; Thompson, J. D. Hall effect in the extremely large magnetoresistance semimetal WTe_2. *Appl. Phys. Lett.* **2015**, *107*, 182411.

(42) Ruszala, P.; Winiarski, M. J.; Samsel-Czekala, M. Dirac-like electronic-band dispersion of $LaSb_2$ superconductor and its counterpart $laagsb_2$. *Acta Physica Polonica: A* **2020**, *138*, 748−751.

(43) Qiao, Y. X.; Tao, Z. C.; Wang, F. Y.; Wang, H.; Jiang, Z. C.; Liu, Z. T.; Cho, S.; Zhang, F. Y.; Meng, Q. K.; Xia, W.; Yang, Y. C.; Huang, Z.; Liu, J. S.; Liu, Z. H.; Zhu, Z. W.; Qiao, S.; Guo, Y. F.; Zhang, H.; Shen, D. Experimental observation of multiple topological nodal structure in $LaSb_2$. *Science China Physics, Mechanics and Astronomy* **2024**, *67*, 247411.

(44) Werthamer, N. R.; Helfand, E.; Hohenberg, P. C. Temperature and purity dependence of the superconducting critical field, H_{c2}. iii. electron spin and spin-orbit effects. *Phys. Rev.* **1966**, *147*, 295−302.

(45) Tinkham, M. *Introduction to Superconductivity*, 2nd ed.; Dover Publications, 2004.

(46) Okamoto, H. Supplemental literature review of binary phase diagrams: Al-Ni, B-Hf, Ca-Sc, Cr-Sc, Fe-Rh, Hf-Mn, La-Sb, Ni-Re, Ni-Sm, Ni-Zr, Sb-Tb, and Ti-Zr. *Journal of Phase Equilibria and Diffusion* **2019**, *40*, 830−841.

(47) Galvis, J. A.; Suderow, H.; Vieira, S.; Bud'ko, S. L.; Canfield, P. C. Scanning tunneling microscopy in the superconductor $LaSb_2$. *Phys. Rev. B* **2013**, *87*, 214504.

(48) Luccas, R. F.; Fente, A.; Hanko, J.; Correa-Orellana, A.; Herrera, E.; Climent-Pascual, E.; Azpeitia, J.; Pérez-Castañneda, T.; Osorio, M. R.; Salas-Colera, E.; Nemes, N. M.; Mompean, F. J.; García-Hernández, M.; Rodrigo, J. G.; Ramos, M. A.; Guillamón, I.; Vieira, S.; Suderow, H. Charge density wave in layered $La_{1-x}Ce_xSb_2$. *Phys. Rev. B* **2015**, *92*, 235153.

(49) O'Leary, E.; Wang, L.-L.; Kushnirenko, Y.; Schrunk, B.; Eaton, A.; Herrera-Siklody, P.; Canfield, P. C.; Kaminski, A. Band Structure and Fermi Surface Nesting in $LaSb_2$, arxiv:2403.17824[cond-mat.strel] (submitted: 2024−03−26) https://arxiv.org/abs/2403.17824 (accessed: 2024−3−26).